Transport Properties and Device Performance of Quasi-One-Dimensional MoS_2 FETs

M. Matić and M. Poljak*
Computational Nanoelectronics Group
Micro and Nano Electronics Laboratory, Faculty of Electrical Engineering and Computing
University of Zagreb, HR-10000 Zagreb, Croatia
*E-mail: mirko.poljak@fer.hr

***Abstract*—We investigated the bandstructure, transport and device properties of semiconducting MoS_2 nanoribbons (MoS_2NR) with hybrid OH-passivated armchair edges using orbitally-resolved *ab initio* Hamiltonians and quantum transport simulations based on Green's functions. The impact of MoS_2NR width scaling on the bandstructure, transmission, bandgap, injection velocity, charge density and ON-state current are analyzed in detail using the ballistic FET model. We find that sub-3 nm-wide and ~15 nm-long MoS_2NR FETs offer low driving currents under 0.43 mA/µm for nFETs and under 0.6 mA/µm for pFETs. Moreover, the current is only weakly modulated by nanoribbon width downscaling due to immunity of the MoS_2NR bandstructure to quantum confinement effects.**

Keywords*—*MoS₂, molybdenum disulfide, quasi-one-dimensional, nanoribbon, quantum transport, Green's function, NEGF, ab initio, DFT, MLWF

I. Introduction

Since the discovery of graphene in 2004, research focus on two-dimensional (2D) materials as potential candidates to replace silicon in future electronic devices is growing exponentially [1]–[3]. Atomically-thin and dangling-bond-free surfaces along with near-ballistic transport properties of some 2D materials are ideal for future field-effect transistors (FETs). After graphene, monolayer molybdenum disulfide (MoS_2) is one of the most studied 2D materials which showed promise due to high stability, compatibility with graphene, and exceptionally high ON/OFF current ratio > 10^8 [4]. The MoS_2 monolayer is a transition metal disulfide (TMD) with a sandwiched S-Mo-S structure, as shown in Fig. 1. Electronic, transport, and device properties of MoS_2 monolayer devices have been studied extensively and it is often used as a benchmark for other 2D materials [5]–[7]. On the other hand, patterning MoS_2 into quasi-one-dimensional (quasi-1D) nanoribbons, which are illustrated in Fig. 1, enables the tuning of electronic and transport properties, with a potential for beneficial adjustment of device properties as well. Although MoS_2 nanoribbons (MoS_2NRs) in armchair and zigzag directions have been studied previously [8]–[10], due to high influence of edge atoms on the device performance and wide range of possible edge passivation atoms, there are still interesting configurations that have not been explored such as MoS_2NRs with hybrid OH-passivated edges. Electronic properties study in [11] of the hybrid OH-passivated MoS_2NRs showed that this edge configuration is the most stable among all studied edge passivation configurations and, therefore, presents an interesting choice for future MoS_2 based nanodevices once fabrication becomes mature enough. Therefore, in this work we study the device performance of the hybrid OH-passivated MoS_2NRs.

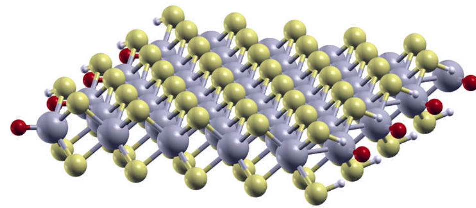

Figure 1. Illustration of an MoS_2 nanoribbon with OH-passivated armchair edges (Mo, S, O and H atoms are represented by grey, yellow, red and white balls, respectively).

Advanced modeling and simulations are used in this study to investigate MoS_2 nanoribbons and MoS_2NR FETs at an atomic level, which is necessary due to inherently strong quantum effects in 2D material nanostructures. Electronic band structure is calculated using the *ab initio* density functional theory (DFT) and, afterwards, maximally-localized Wannier functions (MLWFs) are employed to transform DFT Hamiltonians into a localized basis. The localized MLWF Hamiltonians are much sparser, thus enabling the simulations of realistically sized nanodevice. Quantum transport in such nanostructures is calculated by using the non-equilibrium Greens function (NEGF) formalism. In this paper, we analyze the electronic, transport and device properties of MoS_2NR and MoS_2NR FETs with OH-passivated edges by employing our in-house DFT-NEGF-MLWF solver [12], [13]. We report only a weak impact of MoS_2NR width scaling from ~3.0 nm to ~0.8 nm on the ballistic performance, which results in small degradation and robust performance of ultra-scaled MoS_2NR FETs.

II. Methodology

The MoS_2NR structure of various widths ranging from ~0.8 nm to ~3.0 nm is constructed along the armchair

direction from a MoS_2 unit-cell obtained from Materials Cloud [14] and passivated with OH, as shown in Fig. 1. The Mo edge atoms are passivated with O atoms, while S atoms are passivated with H atoms. Plane-wave DFT is used to obtain highly accurate Hamiltonians of MoS_2 nanostructures investigated in this work. Since DFT calculations assumes periodicity in all three directions, we add a vacuum region of 20 Å in confined directions to exclude any interaction between adjacent layers. For DFT calculations we employ Quantum Espresso [15] with Perdew-Burke-Ernzerhof generalized gradient approximation (PBE-GGA) [16] exchange-correlation (XC) functional and projector augmented wave (PAW) pseudopotentials . The Brillouin zone (BZ) is sampled using an 15-point equally-spaced Monkhorst-Pack grid [17] in the transport direction and a single point in the confined directions. The plane-wave cutoff energy is set to 100 Ry, whereas the convergence threshold is set to 10^{-3} eV/Å for the ionic force and to 10^{-4} eV for energy.

Dense DFT Hamiltonians are localized in energy and are, therefore, not suitable for NEGF quantum transport simulations which prefer sparser matrices, i.e. space-localized Hamiltonians. Transformation into a space-localized basis is performed using the maximally-localized Wannier functions (MLWFs) [18] which results in tight-binding-like sparse matrices. To obtain MLWF Hamiltonians, we use the Wannier90 [19] program. The main inputs of Wannier90 are the trial orbital projections on Bloch manifold, and in this work the trial orbitals for MoS_2NRs are *d* orbitals for Mo atoms and *p* orbitals for O and S atoms. For all MoS_2NR widths the Wannier spread smaller than 2.5 Å^2 per atom is obtained. For each nanoribbon width, MLWF Hamiltonians of a MoS_2NR unit-cell are scaled in the transport direction to construct ~15 nm-long MoS_2NRs.

For quantum transport simulations we use the NEGF formalism [20]–[22], as implemented in our in-house code [12], [13], [23], [24]. Within NEGF, device is modeled with ideal contacts i.e. semi-infinite regions of the same material as the channel using the recursive Sancho-Rubio method [25]. Top-of-the-barrier (ToB) model [26] is used in combination with NEGF to assess ballistic device performance of ultra-scaled MoS_2NR FETs with n- and p-type channels. In ToB ballistic FET simulations, gate equivalent oxide thickness (EOT) is set to 1 nm, while source/drain (S/D) region doping levels are set at 0.01 molar fraction of the MoS_2NR areal atomic density. In all devices we set a common OFF-state current (I_{OFF}) of 10 nA/µm as projected in the International Roadmap for Devices and Systems (IRDS) for high-performance (HP) devices in future CMOS technology nodes [27]. Gate control over the channel in the ToB model devices is assumed ideal and, since no tunneling is included, ideal 60 mV/dec subthreshold slope is obtained in all devices. The ballistic ON-state current (I_{ON}) is extracted when both gate and drain are biased at the supply voltage, i.e. $V_{GS} = V_{DS} = 0.7$ V.

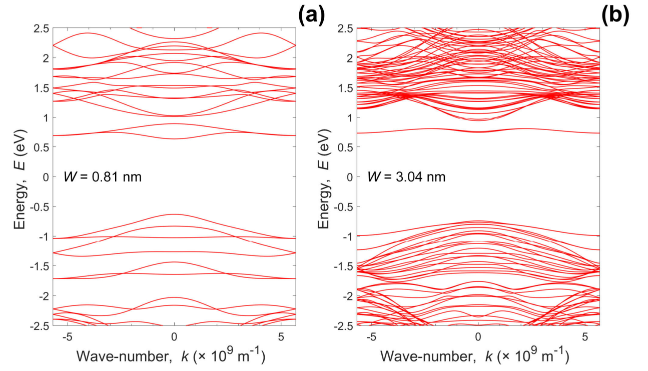

Figure 2. Bandstructure of armchair MoS_2NRs with the widths of (a) 0.81 nm and (b) 3.04 nm.

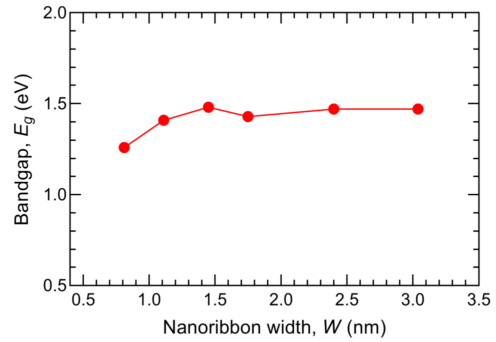

Figure 3. Impact of nanoribbon width scaling on the bandgap of armchair MoS_2NRs.

III. Results and Discussion

In Figure 2 we plot the bandstructure of the widest (Fig. 2a) and the narrowest (Fig. 2b) analyzed MoS_2NR with the widths of $W = 3.04$ nm and $W = 0.81$ nm, respectively. Bandstructure plots contain two subbands that are isolated from the rest of the conduction band (CB). These subbands are isolated due to the influence of edge atoms, which also shift the bandgap from indirect to direct with no conclusive pattern. Scaling down nanoribbon width from 3.04 nm to 0.81 nm results in the separation of these two subbands in CB near the Γ point, which also results in higher curvature, i.e. lower electron effective mass, near CB minimum (CBM) for $W = 0.81$ nm. On the other hand, in the valence band (VB) a higher number of available bands in wider MoS_2NR results in higher number of bands near the VB maximum (VBM), but the narrowest MoS_2NR exhibits a higher curvature and lower hole effective mass in the dominant subband near VBM.

Width-dependence of the bandgap (E_g), extracted from the bandstructure of MoS_2NRs of various widths, is reported in Fig. 3. The plot show a nearly constant bandgap of ~1.47 eV for MoS_2NRs with $W > 1.4$ nm, while scaling down the width below 1.4 nm results in a sharp E_g decrease to 1.26 eV in the 0.81 nm-wide MoS_2NR. The OH-passivated MoS_2NRs exhibit a similar bandgap compared to 2D monolayer MoS_2 for which we obtain the bandgap of 1.7 eV. This value is in line with

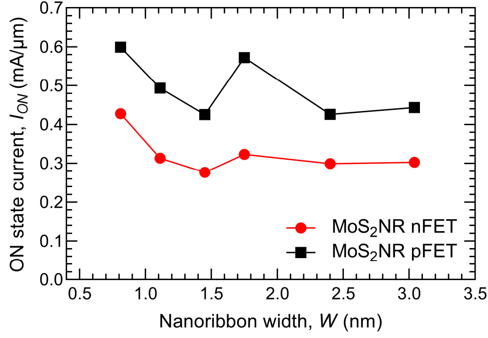

Figure 4. Width-dependence of the ON-state current in n- and p-type MoS_2NR FETs. I_{ON} extracted at $V_{GS} = V_{DS} = V_{DD} = 0.7$ V, with a common I_{OFF} = 10nA set for all devices.

$E_g = 1.67$ eV reported in [11] with the main difference coming from the isolated edge-state bands in the CB.

In order to assess the scaling and confinement effects on device performance, we plot the ON-state current in Fig. 4 for different widths and both device types. Both n- and pFETs exhibit similar scaling laws of I_{ON} with width-downscaling. Qualitatively, we can separate the plot into two groups or two width ranges. The first group includes MoS_2NR FETs with channel widths from $W = 3.04$ nm to $W = 1.75$ nm, which shows increase of I_{ON} while scaling down MoS_2NR width. The second group starts with $W = 1.45$ nm where the I_{ON} shows a sharp decrease compared to the $W = 1.75$ nm case, while further width downscaling results in an increase of I_{ON} down to the 0.81 nm-wide MoS_2NR FET. The maximum I_{ON} for both n- and pFETs is obtained for 0.81 nm-wide MoS_2NR transistor with $I_{ON} = 0.43$ mA/μm for the nFET and $I_{ON} = 0.60$ mA/μm for the pFET. Comparing the obtained I_{ON} results for MoS_2NR FETs to IRDS requirements at the "3 nm" and "2.1 nm" nodes, we conclude that the I_{ON} goal set at 1.9 mA/μm is fulfilled by none of the MoS_2NR devices explored in this paper.

To further understand the behavior of the ON-state current we plot density of states (DOS), transmission, the ON-state charge density (Q_s) and injection velocity (v_{inj}) at ToB, and the ON-state current energy-density. The DOS and transmission characteristics, plotted separately for electrons and holes i.e. in the CB and VB, are shown in Fig. 5. The DOS near the CBM is similar for all MoS_2NRs up to ~0.08 eV after which, due to the existence of isolated edge-state bands, there are no free states and DOS goes to zero. There is an exception for $W = 0.81$ nm where we previously in Fig. 2a observed the broadening of the isolated band near the Γ point. This band broadening results in a nonzero DOS in a broader energy range in comparison to wider nanoribbons. Transmission exhibits similar characteristics as DOS in the CB. At the CBM, transmission equals 1 for the widths of 0.81 nm and 1.75 nm, and sharply increases to 2 at an energy ~20 meV away from the CBM. Interestingly, these MoS_2NRs have a direct bandgap and show highest drain current of all the simulated MoS_2NR nFETs. On the other hand, the 1.45 nm-wide and 3.04 nm-wide MoS_2NRs have a higher transmission equal to 2 at the CBM. This is because these MoS_2NRs have an indirect bandgap with a lower curvature of the CB dispersion, which results in lower I_{ON}. On the other hand, in VB we observe that scaling down nanoribbon width decreases the number of Van Hove

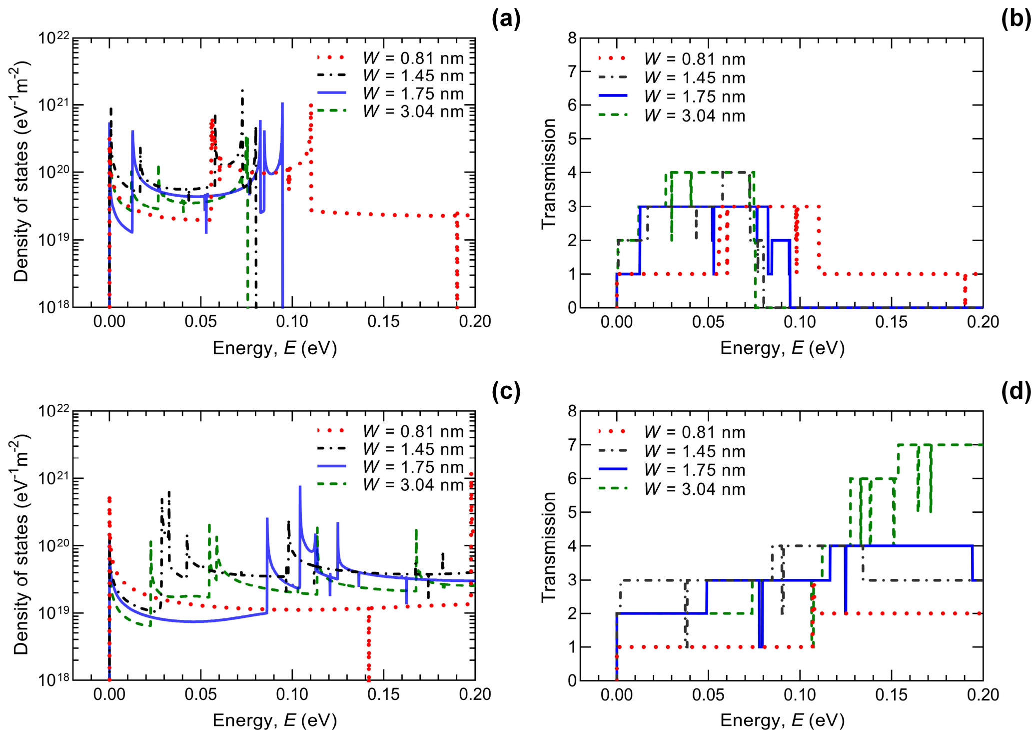

Figure 5. Comparison of DOS (panels on the left) and transmission (panels on the right) in (a, b) CB and (c, d) VB of MoS_2NRs of various widths.

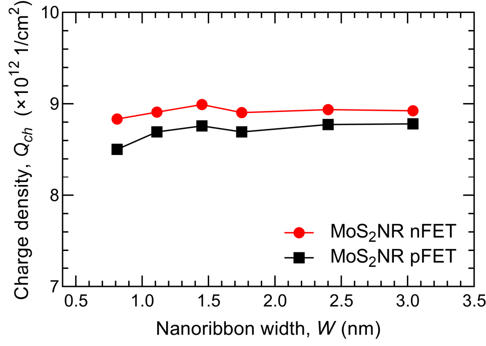

Figure 6. Width-dependence of the channel charge density at ToB in n- and p-type MoS_2NR FETs. The Q_s is extracted in the ON-state, i.e. $V_{GS} = V_{DS} = V_{DD} = 0.7$ V.

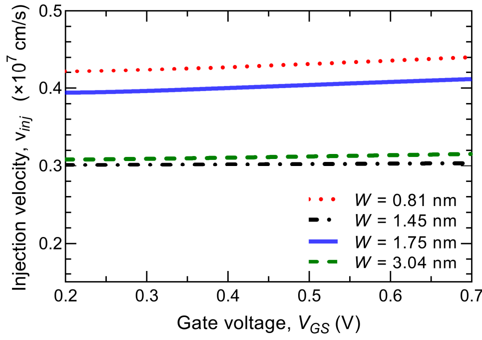

Figure 7. Hole injection velocity dependence on gate bias in MoS_2NR pFETs with various channel widths. $V_{DS} = V_{DD} = 0.7$ V.

singularities (VHS) in the hole DOS near the VBM due to the lower number of available subbands in narrower MoS_2NRs. For the same reason, transmission near the VBM decreases while scaling down MoS_2NR width. When comparing the transport of electrons and holes, we see that holes generally exhibit a higher transmission probability than electrons over the 200 meV energy range away from the VBM or CBM, respectively, which is partly responsible for the higher I_{ON} in p-type than in n-type MoS_2NR FETs reported in Fig. 4.

The DOS and transmission exhibit complex characteristics and are unable to provide a clear insight into FET performance. The influence of width scaling on the ON-state charge density at the ToB is plotted in Fig. 6. Despite considerable variations in the DOS, similar values of Q_s are obtained for all MoS_2NR nFETs and pFETs. On average over all nanoribbon widths, electron density is ~8.9×10^{12} cm^{-2}, while hole density is somewhat lower and equals ~8.7×10^{12} cm^{-2}. The impact of scaling and confinement is visible only in the 0.81 nm-wide MoS_2NRs that show slightly lower electron and hole density at 8.8×10^{12} cm^{-2} and 8.5×10^{12} cm^{-2}, respectively. This decrease is due to setting the common I_{OFF} value, because MoS_2NR with the width of 0.81 nm has the smallest bandgap and, therefore, the lowest applied bias is needed to set I_{OFF} which results in slightly lower Q_s at ToB.

Within the ballistic ToB model, we have $I_{ON} = Q_s \cdot v_{inj}$ at ToB in the ON-state and, hence, the peculiar I_{ON} - W characteristic in Fig. 4 is a consequence of the injection velocity behavior [13], [26]. In Fig. 7 we plot the gate bias dependence of v_{inj} in pFETs, with gate voltage ranging from the threshold voltage (~0.2 V) to supply voltage (0.7 V). Only the v_{inj} in pFETs is plotted because nFETs do not show any noticeable velocity modulation with the applied gate voltage. On the other hand, hole injection velocity in MoS_2NR pFETs with the widths of 0.81 nm and 1.75 nm show a slight increase of v_{inj} with increasing gate bias. The modulation is rather weak, equaling around 5% increase with maximum value obtained in the ON-state of 0.41×10^7 cm/s and 0.44×10^7 cm/s, respectively. With the proportional relationship of the ON-state current to v_{inj} and Q_s, and v_{inj} showing similar scaling laws as I_{ON} while Q_s being of the similar value for all MoS_2NR widths we determine that ON-state performance is dominantly determined by v_{inj}. In comparison to other contending 2D materials, MoS_2NR FETs exhibit significantly lower v_{inj} that deteriorates up to ~9× in comparison to graphene nanoribbons, and ~1.5× when compared against conventional Si MOSFETs [28]. Hence, it is no surprise that the I_{ON} of MoS_2NR FETs is lower than in other 2D material devices [28]–[31].

Finally, the ON-state current energy-density (J_{de}) for MoS_2NR nFET (Fig. 8a) and pFET (Fig. 8b) shows that the current flows mostly in the ~100 meV energy range above/under the CBM/VBM. This range coincides with the energy range of isolated bands in the CB and, therefore, only the isolated edge-state bands in the CB determine the performance of nFETs. On the other hand, VB offers higher number of available bands in the same energy

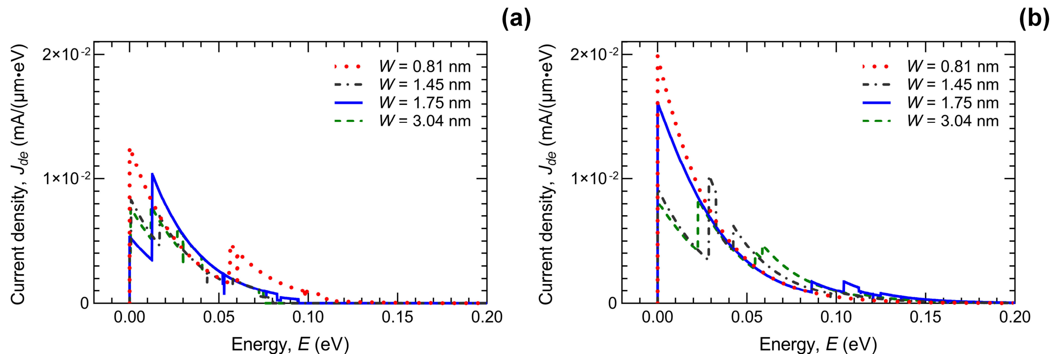

Figure 8. Current energy-density at ToB in the ON-state for MoS_2NR (a) nFETs and (b) pFETs with different nanoribbon channel widths.

range, which results in higher J_{de}, i.e. maxima of 1.2×10^{-2} mA/(eV·µm) for nFETs and 2×10^{-2} mA/(eV·µm) for pFETs, with both values reached at the CBM and VBM, respectively. Hence, any improvement of MoS_2NR nFET performance depends on the effective turn-off of the isolated band contribution.

IV. Conclusions

We studied the electronic, transport and ballistic device characteristics of sub-3 nm-wide and ~15 nm-long quasi-1D MoS_2 nanostructures with OH-passivated edges. We employed DFT and MLWFs to obtain the electronic structure, and NEGF simulations with the ToB model to assess the ballistic performance of armchair MoS_2NR FETs. We found that nFET is limited by the two isolated bands in the CB, which exist due to edge configuration or edge states. The analysis revealed that Q_s is similar for all MoS_2NR widths, and that I_{ON} - W dependence is mainly determined by the features of v_{inj}. The maximum ON-state current of 0.43 mA/µm is obtained for nFETs and 0.6 mA/µm for pFETs. Therefore, MoS_2NR FETs passivated with OH do not meet IRDS requirements for advanced nodes unless a method of eliminating edge states and associated isolated bands in the CB is found.

Acknowledgments

This work was supported by the Croatian Science Foundation under the project CONAN2D (Grant No. UIP-2019-04-3493).

References

[1] K. S. Novoselov *et al.*, "Electric Field Effect in Atomically Thin Carbon Films," *Science*, vol. 306, no. 5696, pp. 666–669, Oct. 2004, doi: 10.1126/science.1102896.

[2] G. Fiori *et al.*, "Electronics based on two-dimensional materials," *Nat. Nanotechnol.*, vol. 9, no. 10, pp. 768–779, Oct. 2014, doi: 10.1038/nnano.2014.207.

[3] N. Briggs *et al.*, "A roadmap for electronic grade 2D materials," *2D Mater.*, vol. 6, no. 2, p. 022001, Jan. 2019, doi: 10.1088/2053-1583/aaf836.

[4] B. Radisavljevic, A. Radenovic, J. Brivio, V. Giacometti, and A. Kis, "Single-layer MoS2 transistors," *Nature Nanotechnology*, vol. 6, no. 3, pp. 147–150, 2011, doi: 10.1038/nnano.2010.279.

[5] W. Cao, J. Kang, D. Sarkar, W. Liu, and K. Banerjee, "Performance evaluation and design considerations of 2D semiconductor based FETs for sub-10 nm VLSI," in *2014 IEEE International Electron Devices Meeting*, Dec. 2014, p. 30.5.1-30.5.4. doi: 10.1109/IEDM.2014.7047143.

[6] A. Nourbakhsh *et al.*, "MoS2 Field-Effect Transistor with Sub-10 nm Channel Length," *Nano Lett.*, vol. 16, no. 12, pp. 7798–7806, Dec. 2016, doi: 10.1021/acs.nanolett.6b03999.

[7] Y. Lee, S. Fiore, and M. Luisier, "Ab initio mobility of single-layer MoS2 and WS2: comparison to experiments and impact on the device characteristics," in *2019 IEEE International Electron Devices Meeting (IEDM)*, Dec. 2019, p. 24.4.1-24.4.4. doi: 10.1109/IEDM19573.2019.8993477.

[8] C. Ataca, H. Şahin, E. Aktürk, and S. Ciraci, "Mechanical and Electronic Properties of MoS2 Nanoribbons and Their Defects," *J. Phys. Chem. C*, vol. 115, no. 10, pp. 3934–3941, Mar. 2011, doi: 10.1021/jp1115146.

[9] K. Dolui, C. D. Pemmaraju, and S. Sanvito, "Electric Field Effects on Armchair MoS2 Nanoribbons," *ACS Nano*, vol. 6, no. 6, pp. 4823–4834, Jun. 2012, doi: 10.1021/nn301505x.

[10] Q. Yue *et al.*, "Bandgap tuning in armchair MoS2 nanoribbon," *J. Phys.: Condens. Matter*, vol. 24, no. 33, p. 335501, Jul. 2012, doi: 10.1088/0953-8984/24/33/335501.

[11] L. Zhang *et al.*, "Modulation of Electronic Structure of Armchair MoS $_2$ Nanoribbon," *J. Phys. Chem. C*, vol. 119, no. 38, pp. 22164–22171, Sep. 2015, doi: 10.1021/acs.jpcc.5b04747.

[12] M. Matić;, T. Župančić, and M. Poljak, "Parallelized Ab Initio Quantum Transport Simulation of Nanoscale Bismuthene Devices," in *2022 45th Jubilee International Convention on Information, Communication and Electronic Technology (MIPRO)*, 2022, pp. 118–123. doi: 10.23919/MIPRO55190.2022.9803335.

[13] M. Matić and M. Poljak, "Ab initio quantum transport simulations of monolayer GeS nanoribbons," *Solid-State Electronics*, vol. 197, p. 108460, Nov. 2022, doi: 10.1016/j.sse.2022.108460.

[14] L. Talirz *et al.*, "Materials Cloud, a platform for open computational science," *Sci Data*, vol. 7, no. 1, Art. no. 1, Dec. 2020, doi: 10.1038/s41597-020-00637-5.

[15] P. Giannozzi *et al.*, "QUANTUM ESPRESSO: a modular and open-source software project for quantum simulations of materials," *J. Phys.: Condens. Matter*, vol. 21, no. 39, Art. no. 39, Sep. 2009, doi: 10.1088/0953-8984/21/39/395502.

[16] J. P. Perdew, K. Burke, and M. Ernzerhof, "Generalized Gradient Approximation Made Simple," *Phys. Rev. Lett.*, vol. 77, no. 18, Art. no. 18, Oct. 1996, doi: 10.1103/PhysRevLett.77.3865.

[17] H. J. Monkhorst and J. D. Pack, "Special points for Brillouin-zone integrations," *Phys. Rev. B*, vol. 13, no. 12, Art. no. 12, Jun. 1976, doi: 10.1103/PhysRevB.13.5188.

[18] N. Marzari and D. Vanderbilt, "Maximally localized generalized Wannier functions for composite energy bands," *Phys. Rev. B*, vol. 56, no. 20, Art. no. 20, Nov. 1997, doi: 10.1103/PhysRevB.56.12847.

[19] G. Pizzi *et al.*, "Wannier90 as a community code: new features and applications," *J. Phys.: Condens. Matter*, vol. 32, no. 16, p. 165902, Apr. 2020, doi: 10.1088/1361-648X/ab51ff.

[20] S. Datta, *Electronic Transport in Mesoscopic Systems*. Cambridge University Press, 1997.

[21] M. Pourfath, *The Non-Equilibrium Green's Function Method for Nanoscale Device Simulation*. Wien: Springer-Verlag, 2014. doi: 10.1007/978-3-7091-1800-9.

[22] Y. He, T. Kubis, M. Povolotskyi, J. Fonseca, and G. Klimeck, "Quantum transport in NEMO5: Algorithm improvements and high performance implementation," in *2014 International Conference on Simulation of Semiconductor Processes and Devices (SISPAD)*, Sep. 2014, pp. 361–364. doi: 10.1109/SISPAD.2014.6931638.

[23] M. Poljak, "Electron Mobility in Defective Nanoribbons of Monoelemental 2D Materials," *IEEE Electron Dev. Lett.*, vol. 41, no. 1, pp. 151–154, Jan. 2020, doi: 10.1109/LED.2019.2952661.

[24] M. Poljak, M. Matić, and A. Zeljko, "Minimum Contact Resistance in Monoelemental 2D Material Nanodevices With Edge-Contacts," *IEEE Electron Device Letters*, vol. 42, no. 8, pp. 1240–1243, Aug. 2021, doi: 10.1109/LED.2021.3087908.

[25] M. P. L. Sancho, J. M. L. Sancho, and J. Rubio, "Quick iterative scheme for the calculation of transfer matrices: application to Mo (100)," *J. Phys. F: Met. Phys.*, vol. 14, no. 5, Art. no. 5, May 1984, doi: 10.1088/0305-4608/14/5/016.

[26] A. Rahman, Jing Guo, S. Datta, and M. S. Lundstrom, "Theory of ballistic nanotransistors," *IEEE Trans. Electron Devices*, vol. 50, no. 9, pp. 1853–1864, Sep. 2003, doi: 10.1109/TED.2003.815366.

[27] "'IEEE Intl. Roadmap for Devices and Systems (IRDS), 2019 Update.' https://irds.ieee.org/."

[28] G. Liang, N. Neophytou, D. E. Nikonov, and M. S. Lundstrom, "Performance Projections for Ballistic Graphene Nanoribbon Field-Effect Transistors," *IEEE Transactions on Electron Devices*, vol. 54, no. 4, pp. 677–682, Apr. 2007, doi: 10.1109/TED.2007.891872.

[29] S. Kaneko, H. Tsuchiya, Y. Kamakura, N. Mori, and M. Ogawa, "Theoretical performance estimation of silicene, germanene, and graphene nanoribbon field-effect transistors under ballistic transport," *Appl. Phys. Express*, vol. 7, no. 3, p. 035102, Mar. 2014, doi: 10.7567/APEX.7.035102.

[30] X. Cao and J. Guo, "Simulation of Phosphorene Field-Effect Transistor at the Scaling Limit," *IEEE Trans. Electron Devices*, vol. 62, no. 2, pp. 659–665, Feb. 2015, doi: 10.1109/TED.2014.2377632.

[31] M. Poljak and M. Matić, "Bandstructure and Size-Scaling Effects in the Performance of Monolayer Black Phosphorus Nanodevices," *Materials*, vol. 15, no. 1, Art. no. 1, Jan. 2022, doi: 10.3390/ma15010243.